

Investigation of the Detection of Shallow Tunnels Using Electromagnetic and Seismic Waves

Tegan Counts, Gregg Larson, Ali Cafer Gürbüz,
James H. McClellan and Waymond R. Scott Jr. *

Georgia Institute of Technology
Atlanta, GA 30332-0250;

ABSTRACT

Multimodal detection of subsurface targets such as tunnels, pipes, reinforcement bars, and structures has been investigated using both ground-penetrating radar (GPR) and seismic sensors with signal processing techniques to enhance localization capabilities. Both systems have been tested in bi-static configurations but the GPR has been expanded to a multi-static configuration for improved performance. The use of two compatible sensors that sense different phenomena (GPR detects changes in electrical properties while the seismic system measures mechanical properties) increases the overall system's effectiveness in a wider range of soils and conditions. Two experimental scenarios have been investigated in a laboratory model with nearly homogeneous sand. Images formed from the raw data have been enhanced using beamforming inversion techniques and Hough Transform techniques to specifically address the detection of linear targets. The processed data clearly indicate the locations of the buried targets of various sizes at a range of depths.

Keywords: Multistatic Imaging, Ground penetrating radar (GPR), tunnel detection, beamforming, Hough Transform

1. INTRODUCTION

In recent years, there has been increased interest in the detection of subsurface objects that are linear in structure, such as tunnels and pipes, for homeland security concerns. These targets may be detected using ground-penetrating radar (GPR) and seismic techniques.¹⁻³ Because these sensing modalities detect changes in distinctly different phenomena, it is reasonable to hypothesize that combining them into a unified multi-modal system will result in improved target detection and localization. Enhancements are also possible through signal processing to take advantage of the linear nature of the targets. Additionally, other types of targets can be detected using similar methods. To seismically detect the presence of buried targets such as tunnels, a compressional wave is excited in the ground by an acoustic wave from an aero-acoustic source positioned above the surface as shown in Fig. 1(a). As the compressional wave propagates into the soil, it interacts with buried targets, resulting in reflected and scattered waves which can be measured at the surface using either ground-contacting or non-contacting sensors.⁴⁻¹⁰ The surface motion, which is indicative of the changes in the mechanical properties of the ground, can then be used to localize buried targets either from the raw data or after post-processing using back-projection methods.^{2,11} Two GPR antennas can be operated similarly in a bi-static mode with one antenna operating as a transmitter and the other operating as a receiver. To expand the sensor's capabilities, multiple pairs of GPR antennas may be operated in a multi-static mode as shown in Fig. 1(b). With two transmitters and four receivers, eight different antenna pairs can be used to measure changes in the ground's electrical properties. The individual measurements from each antenna pair provide a wide range of target aspect angles that can be combined to reduce clutter levels in the images.

Two different experimental scenarios have been investigated with scale models of linear structures in a tank filled with nearly-homogeneous sand as shown in Fig. 2. To simulate a single shallow tunnel, a 3-m long, 10-cm diameter, corrugated drainage pipe was buried approximately 58 cm deep in the model. The pipe ran parallel to the y -axis and extended outside of the scan region as shown in Fig. 2(a). To investigate a more difficult

This work is supported under MURI by the U.S. Army Research Office under contract number DAAD19-02-1-0252
Further author information: (Send correspondence to Ali Cafer Gürbüz): E-mail:alicafer@ece.gatech.edu

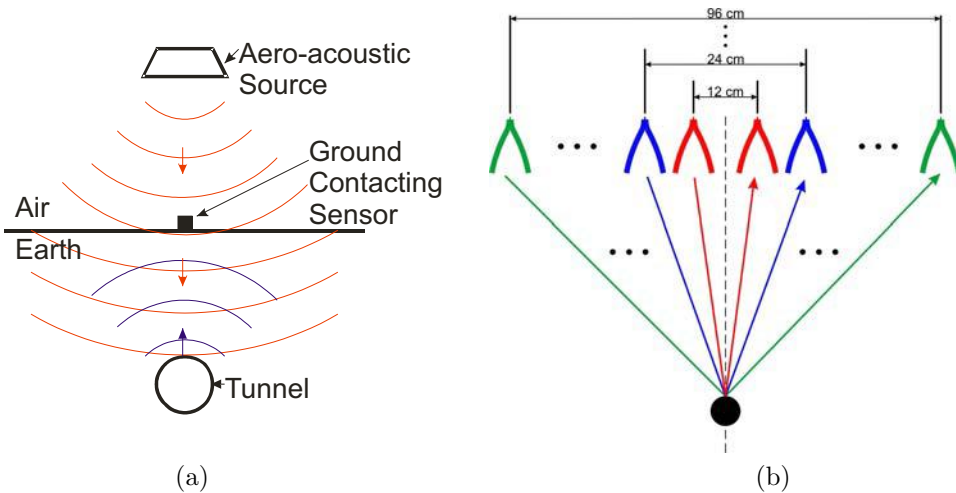


Figure 1. Diagrams depicting the wave propagation for a) the seismic system, and b) the multi-static GPR system

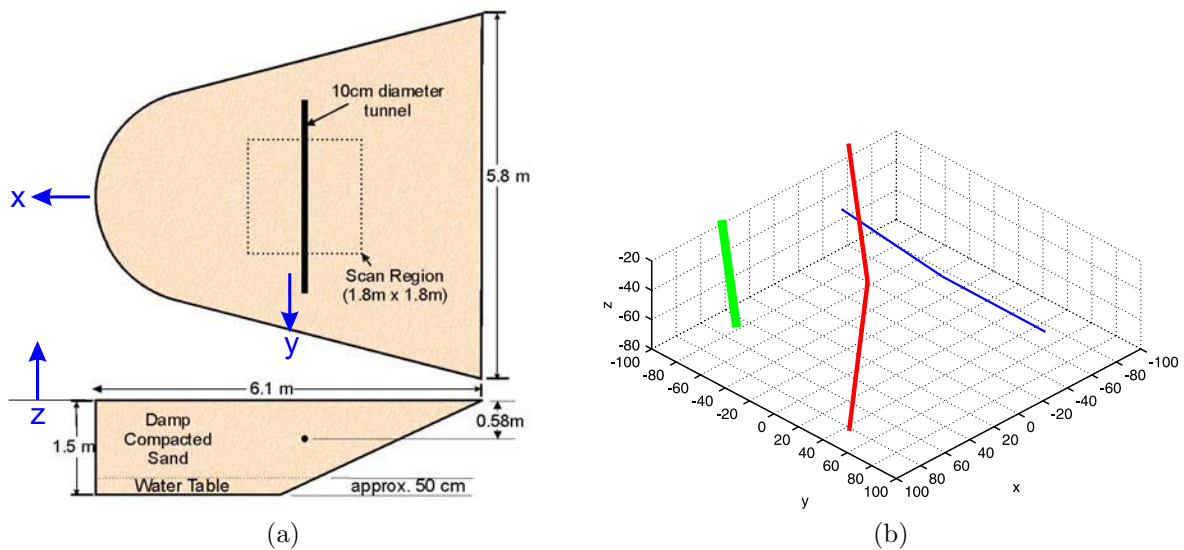


Figure 2. (a) Model of the sand tank with one 10-cm tunnel buried approx 58 to 60 cm from the surface. (b) Layout of the three buried PVC pipes. The targets are a 5.08-cm pipe buried approx 30 cm deep, a 2.54-cm pipe buried diagonally from the surface down to 60 cm, and a 1.27-cm pipe buried approx 60 cm deep. The coordinate system is the same in both (a) and (b).

configuration, three PVC pipes with diameters of 1.27cm, 2.54 cm, and 5.08 cm were buried with variable depths in the model as shown in Fig. 2(b) for the second scenario. In the following sections, the GPR and seismic sensors, measured data, and post-processed imaging results from beamforming and Hough Transform techniques will be presented for the two experimental scenarios.

2. EXPERIMENT 1

2.1. Acoustic Experiment

Seismic and multistatic GPR antenna array sensors were assembled, as shown in Fig. 3, for experimental testing in the two scenarios shown in Fig. 1. The seismic sensor used a VIFA P13WH-00-08 midwoofer in a VIFA M13 enclosure as the aero-acoustic source and the accelerometer in a PCB Piezotronics impedance head (Model 288D01) mounted on a Brüel and Kjaer electrodynamic modal exciter (Model 4810) with a 3.2-cm diameter,

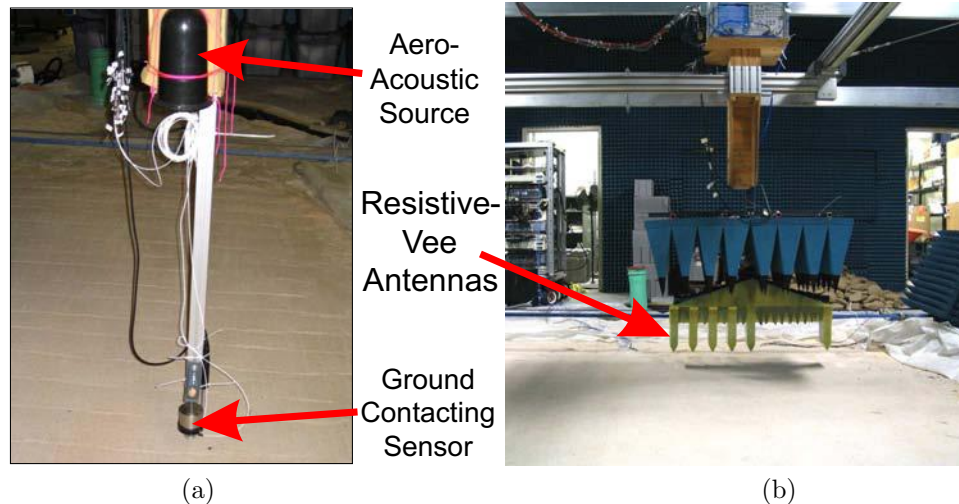


Figure 3. Photographs of the experimental setups of a) the seismic system and b) the multi-static GPR.

0.64-cm thick, aluminum foot in direct contact with the ground as the sensor. The midwoofer was positioned 103 cm above the soil surface as seen in Fig. 3 to preferentially excite plane waves at the ground surface; the radial distance between the centerline of the source and the centerline of the sensor was 16.1 cm. A Behringer ECM8000 microphone, shown to the right of the impedance head in Fig. 3, measured the pressure of the incident signal at the surface; the microphone was offset 9.7 cm from the accelerometer. The source and sensors were scanned over a $1.8 \text{ m} \times 1.8 \text{ m}$ region in a raster fashion in 4-cm increments by an automated positioning system. Data acquisition and signal generation were accomplished at 32,000 points/second with a 4 second chirp excitation over frequencies from 100 Hz to 8 kHz. The chirp excitation was low-pass filtered at 8 kHz with appropriate amplification. The measured acceleration was filtered in two stages with the first being a low-pass filter at 8 kHz and the second being a band-pass filter between 100 Hz and 10 kHz. The measured pressure was low-pass filtered at 8 kHz and high-pass filtered at 80 Hz and at 150 Hz in three different stages. The measured signals were amplified as necessary for data acquisition. Compression of the data using a 3.6 kHz center frequency differentiated Gaussian pulse in the post-processing results in the hyperbolic tunnel signature seen in the representative data shown in Fig. 4 for $y = -62 \text{ cm}$, $y = -2 \text{ cm}$, $y = 66 \text{ cm}$, and $x = -14 \text{ cm}$. The data are shown over the full range of x (-90 cm to 90 cm , shown on the abscissa) as a function of time (from 2 to 16 ms, shown on the ordinate). The interaction of the incident signal with the ground surface is shown as a line across the entire image at approximately 3.8 ms. The sloping bottom of the sand tank can also be seen as a straight line that slopes downward at the right side of the image. In the following signal processing section, these images have been enhanced using back-propagation techniques.

2.2. Multi-static GPR

The multi-static GPR (Fig. 3(b)) consists of a linear array of resistive-vee antennas. The resistive-vee is chosen because it can radiate short pulses and has a low radar cross section.¹²⁻¹⁴ There are two transmitters (T1, T2) and four (R1, R2, R3, and R4) receivers in the array; they combine to form eight bi-static separations ranging from 12 cm to 96 cm in 12 cm increments (Fig. 1). Microwave absorber is strategically placed on the array to reduce coupling between antennas and reflections between the array and the ground. The array is scanned over a $1.8 \text{ m} \times 1.8 \text{ m}$ region by a automated positioner in 2-cm increments. At each position, a vector network analyzer measures the 401 point frequency response of each pair over the range of 60 MHz to 8.06 GHz. Microwave switches make it possible for one analyzer to obtain data from all eight pairs. A test PC controls this entire process.

The lowest effective frequency is in the range of 500 MHz to 1.0 GHz because the gain of the antenna falls off quickly in this frequency range.¹⁵ For buried targets, the upper useful frequency is limited by attenuation in the sand. The Fourier transform of a differentiated Gaussian pulse centered at 2.5 GHz was empirically

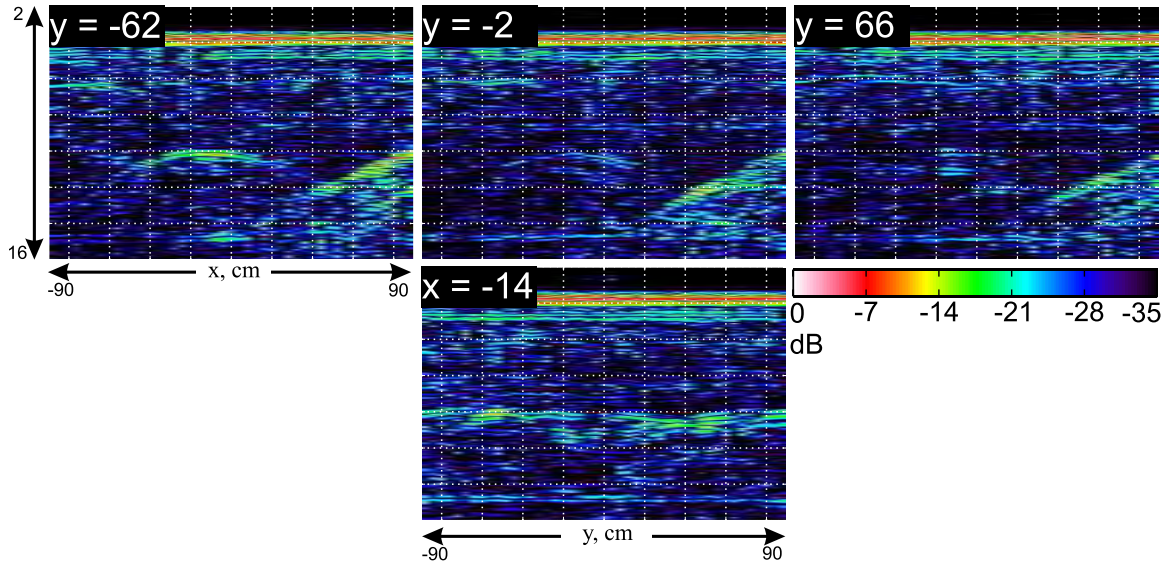


Figure 4. Time-domain, 2-D cuts of the raw seismic data taken at $y=-62$ cm, $y=-2$ cm, $y=66$ cm, and $x=-14$ cm. The vertical axis is time (ms) in each image. All images are on a 35-dB scale, with each normalized to the same maximum.

chosen to window the sub-surface data in the frequency domain. The measured responses contain delays and attenuation in the signal cable, direct coupling between the antennas, etc. To eliminate these artifacts, a simple calibration procedure is applied. A thru measurement is performed on each bi-static pair by removing the antennas, replacing them with a reference cable, and measuring the responses. A free-space measurement is performed by reattaching the antennas and measuring the response of the array when it is pointed at the corner of a room lined with microwave absorber. Then, the measured data are calibrated as

$$\text{TR}(f, x_{ant}, y_{ant}, p) = \frac{\text{RAW}(f, x_{ant}, y_{ant}, p) - \text{FREE}(f, p)}{\text{THRU}(f, p) e^{-j2\pi f t_d}}, \quad (1)$$

where $p = 1, 2, \dots, 8$ are the eight bi-static pairs, f is the frequency, x_{ant} and y_{ant} are the coordinates of the array, and t_d is the combined delay through the reference cable as well as the transmitter and receiver baluns ($t_d = t_{cable} - 2t_{balun}$). This removes the direct coupling between the antennas, the reflections from objects that are near the antenna array, the delay and attenuation in the signal cable, and the effect of the reference cable. It also moves the phase reference from the connector at the end of the antenna package to the other side of the balun. Both $t_{cable} = 7.27$ ns and $t_{balun} = 580$ ps were measured experimentally.

The results of the data acquisition and the above calibration steps are given in Figs. 5 and 6. The data was transformed into the time-domain for display in these figures. The 10-cm tunnel is clearly visible, and it has the same hyperbolic response that is common to synthetic aperture data.

3. SIGNAL PROCESSING

3.1. Imaging Algorithm

The seismic data is imaged by delay-sum backprojection¹⁶ in the time-domain. This technique was chosen because it is straightforward, takes advantage of the synthetic aperture, and can easily and precisely account for the bi-static source-receiver spacings. The air-ground interface is accounted for by an approximation to Snell's law. The wave velocities in the air and sand are estimated to be 340 m/s and 220 m/s, respectively. A synthetic aperture is formed by summing the contributions from many measurement points at each image point. The results of the processing are given in Fig. 7. The processing clearly reduces the background clutter levels while focusing the target response. The ramp at the side of the sand tank appears in these images too.

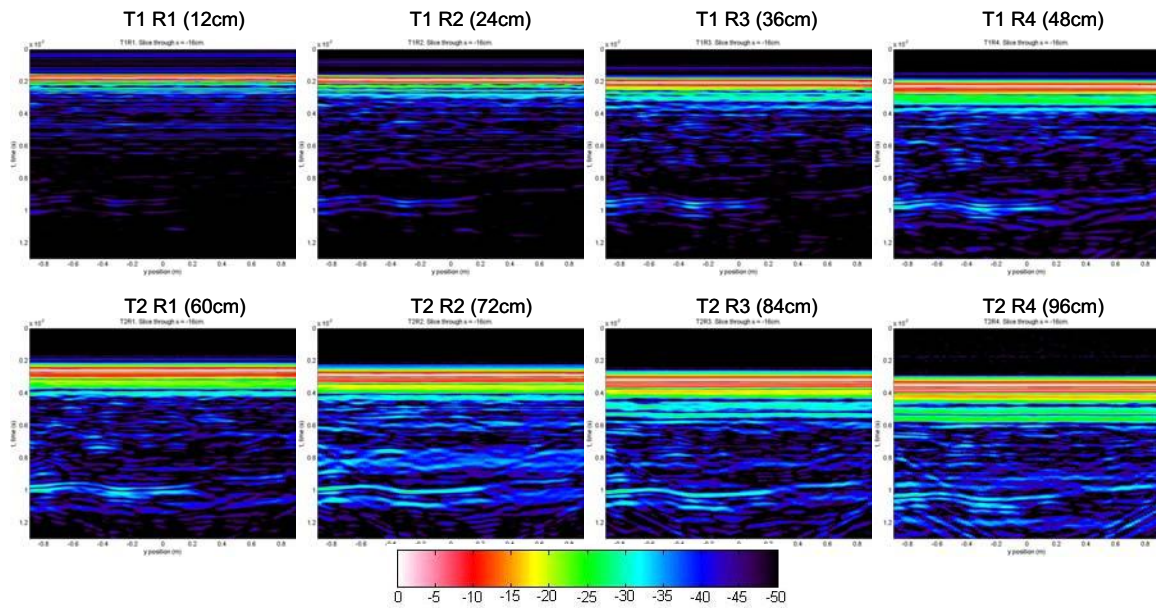


Figure 5. Time-domain, 2-D cuts of the raw GPR data taken at $x = -16$ cm. The vertical axis is time in each image (0 to 1.25 ns). The horizontal axis is the y-dimension ranging from -70 cm to 70 cm. All images are on a 50-dB scale, with each normalized to its own maximum.

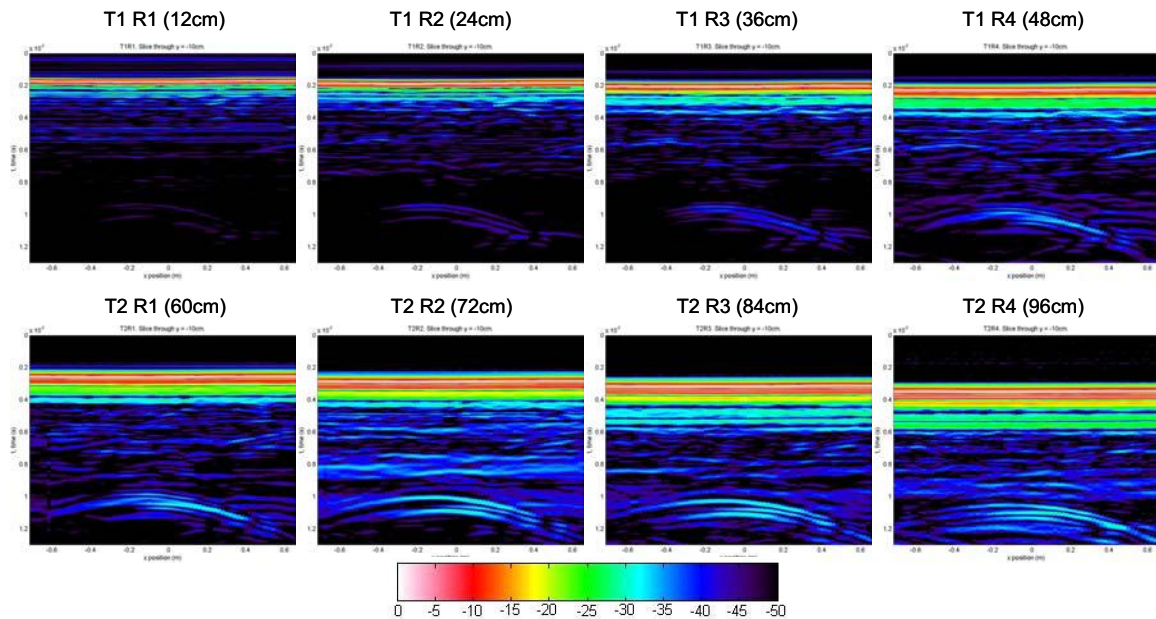


Figure 6. Time-domain, 2-D cuts of the raw GPR data taken at $y = -10$ cm. The vertical axis is time in each image (0 to 1.25 ns). The horizontal axis is the x-dimension ranging from -70 cm to 70 cm. All images are on a 50-dB scale, with each normalized to its own maximum.

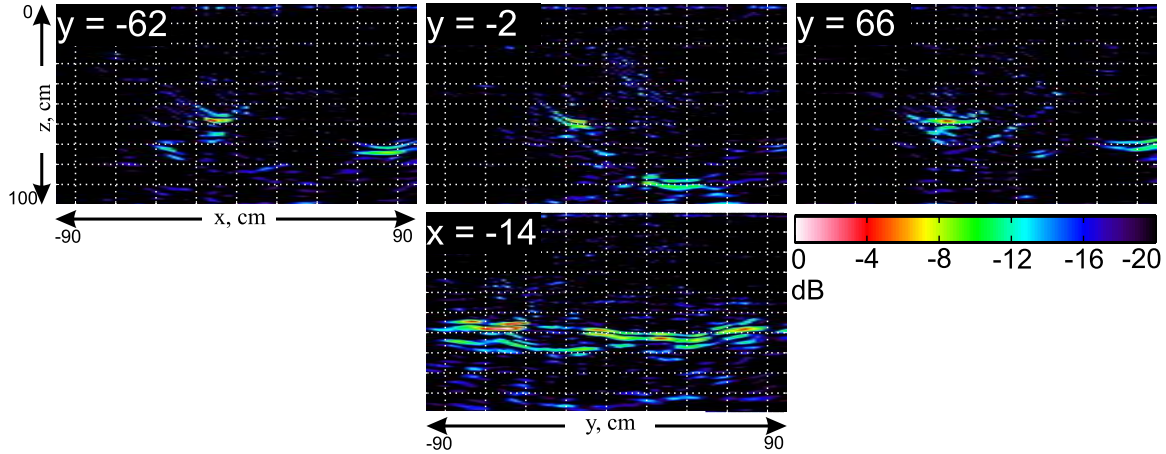


Figure 7. 2-D cuts of the backprojected seismic data taken at $y=-62$ cm, $y=-2$ cm, $y=66$ cm, and $x=-14$ cm. All images are on a 20 dB scale, with each normalized to the same maximum.

The GPR data has been imaged by a beamforming algorithm (2) which is the frequency-domain equivalent of delay-sum backprojection in the time-domain.¹⁶ The GPR is imaged in the frequency-domain because the resistive-vee antenna cannot be characterized by a phase center; the correction, which is not easily implemented in the time-domain, is to correct for the phase response of the antennas. The antenna phase response is a function of both frequency and look angle, and it is obtained by modeling the antenna in a method of moments numerical code.

$$Image(x, y, z, p) = \sum_{x_{ant}} \sum_{y_{ant}} W(\bullet) \sum_f A(f) \frac{TR(f, x_{ant}, y_{ant}, p)}{e^{j\phi_{trans}(f, \bullet)} e^{-j\omega t_t(\bullet)} e^{-j\omega t_r(\bullet)} e^{j\phi_{rcvr}(f, \bullet)}} \quad (2)$$

The phase angles ϕ_{trans} and ϕ_{rcvr} in (2) are the phases of the radiation pattern at the look angle of the propagation path (fig. 8). The terms t_t and t_r in (2) and fig. 8 are the travel times along the wave propagation path between the target and the transmitter/receiver. The travel times are dependent on the length of the propagation path and the propagation velocity in each medium. The travel paths are calculated based on a two-layer ground model.¹ A constant velocity is assumed in each layer: $v_{air} = 2.998 \times 10^8$ m/s, $v_{sand} = 1.50 \times 10^8$ m/s. The sand velocity was determined empirically using moveouts; the velocity was adjusted until the beamformed moveout of a buried target showed alignment across all pairs.¹⁷ An approximation to Snell's law is used to determine the refraction points.^{1, 18} $W(\bullet)$ is an aperture weighting function,

$$W(\bullet) = \sqrt{\frac{\cos(\theta_t) \cos(\theta_r)}{r_t r_r}} \quad (3)$$

where θ_t and θ_r are the polar angles between $-\hat{z}$ and the rays from the transmitter and receiver to the image pixel. The frequency window, $A(f)$, is the Fourier transform of a differentiated Gaussian pulse centered at 2.5 GHz. The synthetic aperture is implemented by summing the contributions from many aperture locations (x_{ant}, y_{ant}) to form each image pixel (x, y, z) . This will improve cross-range resolution. Range resolution is improved by summing over frequency. The (\bullet) represents a dependency on pixel location, antenna location, and pair number.

Note that the values calculated for $Image(x, y, z, p)$ are complex numbers. The real part of this image is what is normally obtained using the standard time-domain backprojection algorithm; it is comparable to the results obtained for the seismic images. The magnitude of the complex image can be viewed as the envelope of the standard time-domain backprojection algorithm; GPR images will all be magnitude images. The processing results for the GPR data are given in Figs. 9 and 10. The tunnel is focused well by all pairs. The response is the

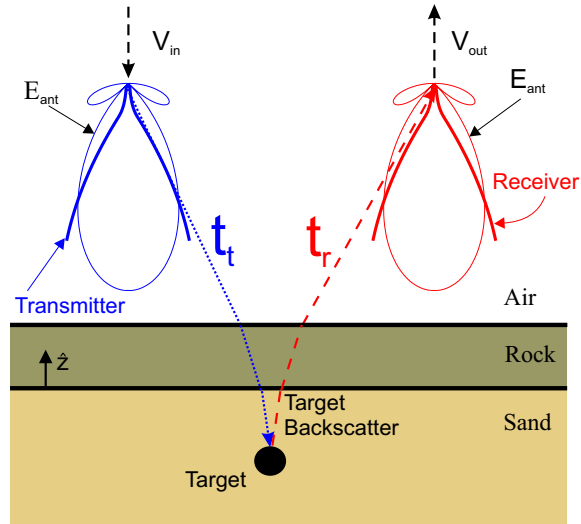


Figure 8. Beamforming model. The propagation path from the transmitter to the target is the dotted line; object to receiver is the dashed line. The radiation patterns in this figure are not the actual patterns; for actual patterns, see.¹⁵

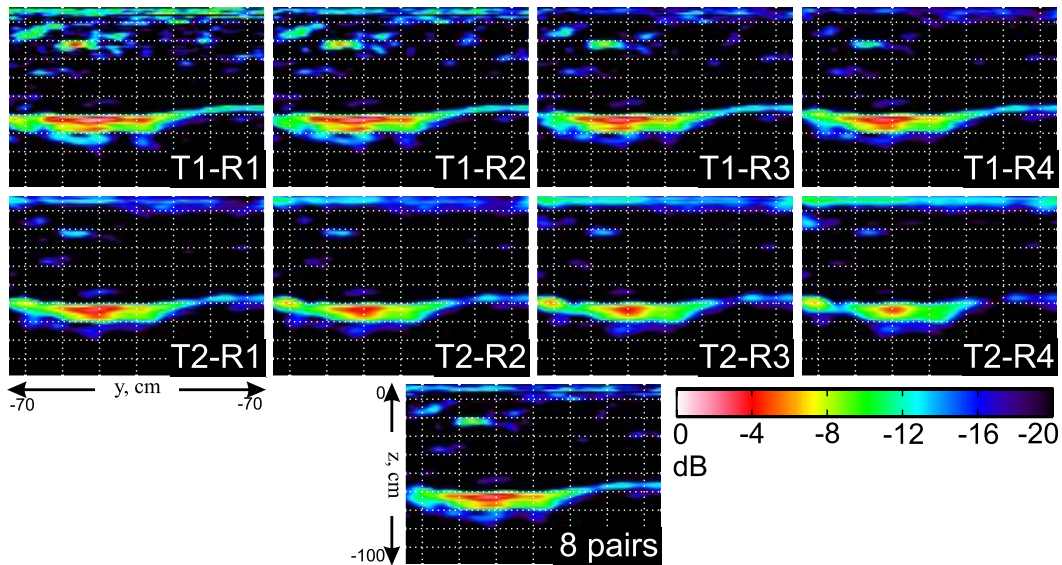


Figure 9. 2-D processed image slices of GPR data from each of the eight bi-static pairs and the multi-static combination. All images range from -70 cm to 70 cm in the y dimension (horizontal axis) and from 0 cm to 100 cm in the z dimension (vertical axis). Each pair is normalized to its own maximum; all images are on a 20-dB scale.

strongest for the narrower pairs; conversely, the clutter level seems to drop in the wider pairs. The multi-static combination images, however, maintain the strong target response while still reducing the clutter. The seismic (fig. 7) and GPR (figs. 9 and 10) results are similar, yet each image has different strong regions that vary slightly from the others. This result encourages the combination of the two modalities.

Since it can be difficult to evaluate the quality of a 3-D image in a 2-D plane cut, Fig. 11 shows 3-D isofigures of the target for bi-static and multi-static GPR results. The results of the Hough Transform (Sec. 3.2) are plotted along with the images. Here, the reduced clutter levels in the eight-pair combination image are obvious and significant. Both isolevels are 15-dB below the maximum response of its own 3-D image space.

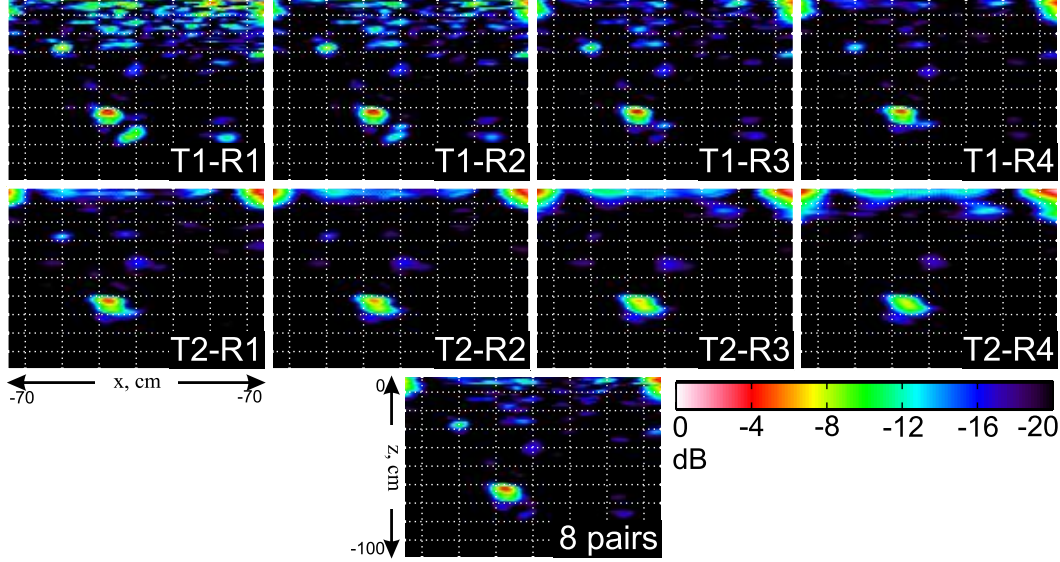


Figure 10. 2-D processed image slices of GPR data from each of the eight bi-static pairs and the multi-static combination. All images range from -70 cm to 70 cm in the x dimension (horizontal axis) and from 0 cm to 100 cm in the z dimension (vertical axis). Each pair is normalized to its own maximum; all images are on a 20-dB scale.

3.2. Hough Transform

The Hough Transform (HT)¹⁹ parameterizes a line and maps the line in the image domain to a single point in the parameter domain. The Hough transform of a digital image $f(x, y)$ using the slope-intercept parametrization of a line is defined as follows:

$$R(m, n)[f(x, y)] = \int_{-\infty}^{\infty} f(x, mx + n) dx \quad (4)$$

where m and n are the slope and the intercept of the line, respectively. Since parameterized lines correspond to peaks in Hough space the problem of tunnel detection is converted to a problem of detecting the corresponding peak for the tunnel in the Hough space. Here, for the specific application of tunnel imaging and detection, we model tunnels as lines over extended distances which allows us to use the HT.

We are interested in the 3D position of a linear feature in subsurface images; thus a 3D Hough Transform is needed. A line in 3D can be parameterized as

$$r = s\tau + u\alpha + v\beta \quad (5)$$

where s is a free parameter and $(\tau \ \alpha \ \beta)$ is an orthobasis for 3D given as

$$\begin{pmatrix} \tau & \alpha & \beta \end{pmatrix} = \begin{pmatrix} \cos \phi \cos \theta & -\sin \theta & -\cos \theta \sin \phi \\ \cos \phi \sin \theta & \cos \theta & -\sin \theta \sin \phi \\ \sin \phi & 0 & \cos \phi \end{pmatrix} \quad (6)$$

Then 3D Hough Transform can be given as

$$H_g(\theta, \phi, u, v) = \int_{-\infty}^{\infty} g(s\tau + u\alpha + v\beta) ds \quad (7)$$

The isofigures in Fig. 11 demonstrate the results of the HT. Although both cases are relative simple, they confirm that the peaks in H_g are at the correct locations.

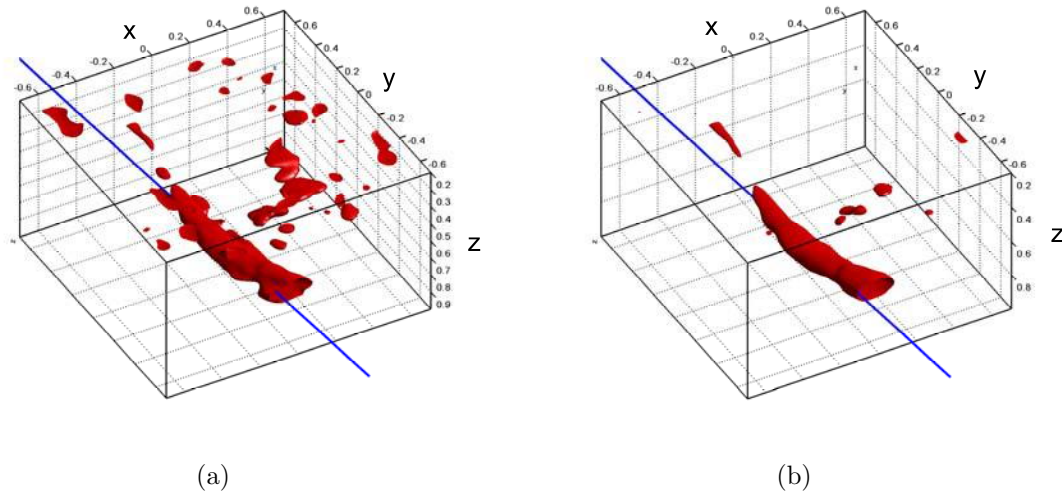


Figure 11. 3-D isofigures at -15 -dB of the 10-cm tunnel using a) one bi-static pair (12-cm spacing) and b) the combination of eight bi-static pairs. The images extend from -70 cm to 70 cm in x and y and from 20 cm deep to 100 cm deep in z .

4. EXPERIMENT 2

The 10-cm single target case was clearly imaged by both modes of detection, and it was easily detected by the Hough Transform. In order to explore the capabilities of the detection systems, a more difficult experiment of linear targets was created (see Fig. 2(b)). At present, only the GPR has been scanned over this scenario, but future seismic work will follow.

The goal of the scenario is to establish the current limits of the system and explore how to expand them. For now, the 1.27 cm diameter pipe at a depth of 60 cm is hard to see with the GPR, so it was filled with water to produce stronger electromagnetic wave reflections. Isofigures at -15 -dB for the processed bi- and multi-static GPR are in Fig. 12. The clutter level in the bi-static image is too high to clearly see the targets, but the eight-pair combination image is relatively clear. The HT is not able to find the deep 1.27-cm pipe in the bi-static data, but it does find all three in the multi-static image. There is one false-alarm in the HT for the multi-static case, but an observation of the image would quickly rule this out as an actual linear target.

5. CONCLUSIONS

The combined multi-static GPR and seismic detection experiments successfully located linear targets, and the Hough Transform was successful in identifying the targets in the imaged results. Beamforming of the measured data significantly improved the target signatures for all experiments. The multi-static combination of the GPR antennas was a crucial step in separating the targets from the clutter. The seismic and GPR images have distinct features which indicate that multi-modal detection will yield better results. In the future, the seismic experiment will also be tested on the three-pipe scenario to determine whether a small and deeply buried pipe can be detected. Other scenarios will be created that introduce clutter, perhaps in layers, to model the most difficult real-world applications.

REFERENCES

1. A. C. Gurbuz, T. Counts, K. Kim, J. McClellan, and W. R. Scott, Jr., "Application of multi-static inversion algorithms to landmine detection," in *Detection and Remediation Technologies for Mines and Minelike Targets XI, Proc. SPIE*, **6217**, May 2006.
2. A. C. Gurbuz, J. H. McClellan, W. R. Scott, Jr, and G. D. Larson, "Seismic tunnel imaging and detection," in *IEEE International Conference on Image Processing*, October, 2006.

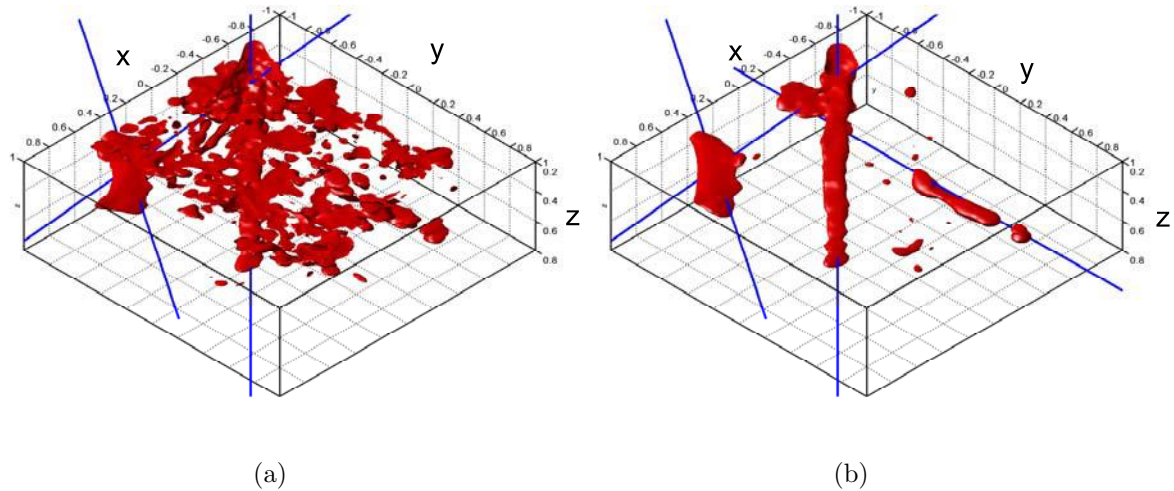


Figure 12. Isofigures at -15 -dB for (a) the bi-static (pair T1-R1, 12-cm separation) and (b) the multi-static combination of all eight pairs. Each figure was normalized to its own maximum, and the isolevel was chosen relative to that maximum in each case. The images extend from -1 m to $+1$ m in x and y and from 20 cm deep to 80 cm deep in z .

3. Kangwook Kim, A. C. Gurbuz, W. R. Scott, Jr., and J. H. McClellan, "A multi-static ground-penetrating radar with an array of resistively-loaded vee dipole antennas for landmine detection," in *Detection and Remediation Technologies for Mines and Minelike Targets X*, Proc. SPIE, **5794**, Mar. 2005.
4. W. R. Scott, Jr, J. S. Martin, and G. D. Larson, "Experimental model for a seismic landmine detection system," *IEEE Journal on Geoscience and Remote Sensing* **36**, pp. 1155–1164, 2001.
5. J. S. Martin, G. D. Larson, and W. R. Scott, Jr, "An investigation of surface contacting sensors for the seismic detection of buried landmines," *Journal of the Acoustical Society of America* **120**(5), pp. 2676–2685, 2006.
6. J. S. Martin, D. J. Fenneman, F. Codron, P. H. Rogers, W. R. Scott, Jr, G. D. Larson, and G. S. McCall II, "Ultrasonic displacement sensor for the seismic detection of buried land mines," in *Detection and Remediation Technologies for Mines and Minelike Targets X*, Proc. SPIE, **4742**.
7. A. G. Petculescu and J. M. Sabatier, "Air-coupled ultrasonic sensing of grass-covered vibrating surfaces; qualitative comparisons with laser Doppler vibrometry," *Journal of the Acoustical Society of America* **115**(4), pp. 1557–1564, 2004.
8. N. Xiang and J. M. Sabatier, "An experimental study on antipersonnel landmine detection using acoustic-to-seismic coupling," *Journal of the Acoustical Society of America* **113**(3), pp. 1333–1341, 2003.
9. D. Donskoy, A. Ekimov, N. Sedunov, and M. Tsionskiy, "Nonlinear seismo-acoustic land mine detection and discrimination," *Journal of the Acoustical Society of America* **111**(6), pp. 2705–2714, 2002.
10. G. D. Larson, J. S. Martin, and W. R. Scott, Jr, "Detection of buried landmines using seismic waves and microphones," in *Detection and Remediation Technologies for Mines and Minelike Targets X*, Proc. SPIE, **5794**.
11. W. R. Scott, Jr., Kangwook Kim, G. D. Larson, A. C. Gurbuz, and J. H. McClellan, "Combined seismic, radar, and induction sensor for landmine detection," in Proc. IEEE Int. Geosci. Remote Sensing Symposium, pp. 1613–1616, September 20–24, 2004.
12. Kangwook Kim and W. R. Scott, Jr., "Design and realization of a discretely loaded resistive vee dipole for ground-penetrating radars," *Radio Science* **39**(4), July 2004.
13. K. Kim and W. R. Scott, Jr., "Design of a resistively-loaded vee dipole for ultra-wideband ground-penetrating radar applications," *IEEE Journal on Antennas and Propagation* **53**, pp. 2525–2532, Aug 2005.
14. T. P. Montoya and G. S. Smith, "Land mine detection using a ground-penetrating radar based on resistively loaded vee dipoles," **47**(12), pp. 1795–1806, 1999.

15. Kangwook Kim and W. R. Scott, Jr., "A resistive linear antenna for ground-penetrating radars," in *Detection and Remediation Technologies for Mines and Minelike Targets IX*, *Proc. SPIE*, **5415**, pp. 359–370, April 2004.
16. X. Feng and M. Sato, "Pre-stack migration applied to GPR for landmine detection," *Inverse Problems* **20**, pp. S99–S115, 2004.
17. D. Leparoux, D. Gibert, and P. Cote, "Adaptation of prestack migration to multi-offset ground-penetrating radar data," *Geophysical Prospecting* **49**, pp. 374–386, 2001.
18. E. Johansson and J. Mast, "Three dimensional ground penetrating radar imaging using a sythetic aperature time-domain focusing," in *Advanced Microwave and Millimeter Wave Detectors*, *Proc SPIE*, **2275**, pp. 205–214, 1994.
19. P. Hough, "A method and means for recognizing complex patterns," *US Patent* (3069654), 1962.